Journal of Energy Chemistry 66 (2022) 597–602

Contents lists available at ScienceDirect

Journal of Energy Chemistry

journal homepage: www.elsevier.com/locate/jechem

http://www.journals.elsevier.com/journal-of-energy-chemistry/

Achieving high conversion of syngas to aromatics

Yi Fu [a,b,c], Youming Ni [a,b], Zhiyang Chen [a,b], Wenliang Zhu [a,b,*], Zhongmin Liu [a,b,c,*]

[a] National Engineering Laboratory for Methanol to Olefins, Dalian Institute of Chemical Physics, Chinese Academy of Sciences, Dalian 116023, Liaoning, China
[b] Dalian National Laboratory for Clean Energy, Dalian Institute of Chemical Physics, Chinese Academy of Sciences, Dalian 116023, Liaoning, China
[c] University of Chinese Academy of Sciences, Beijing 100049, China

ARTICLE INFO

Article history:
Received 15 January 2021
Revised 12 March 2021
Accepted 17 March 2021
Available online 1 April 2021

Keywords:
Syngas
Aromatics
$Fe/ZnCr_2O_4$ oxide
H-ZSM-5 zeolite
High conversion

ABSTRACT

Realizing high CO conversion and high aromatics selectivity simultaneously in syngas-to-aromatics (STA) reaction is still challenging. Herein, we report a 57.5% CO conversion along with 74% aromatics selectivity over a composite catalyst consisting of $Fe/ZnCr_2O_4$ (Fe modified $ZnCr_2O_4$ spinel) oxide and H-ZSM-5 zeolite. Impregnation of only 3 wt% of Fe onto $ZnCr_2O_4$ can remarkably increase CO conversion without sacrificing the aromatics selectivity. Oxygen vacancy concentration is improved after impregnating Fe. The highly dispersed iron carbide species is formed during the reaction over $Fe/ZnCr_2O_4$ spinel oxide. The synergistic effect of oxygen vacancy and iron carbide results in a rapid formation of abundant oxygenated intermediate species, which can be continuously transformed to aromatics in H-ZSM-5. This study provides a new insight into the design of highly efficient catalyst for syngas conversion.

1. Introduction

Aromatics, acting as important building-block chemicals, are widely utilized in fuel additive and the production of pigments, medicines, polymers, solvents, etc [1]. Traditionally, aromatics are primarily acquired through oil cracking and naphtha catalytic reforming, both of which rely on petroleum resources heavily [2,3]. On account of the gradual shortage of petroleum feedstock and the growing requirement for aromatics, developing an alternative route to produce aromatics from non-petroleum resources (such as coal, natural gas, and biomass), is urgent and significant. Syngas (CO and H_2) can be derived from aforementioned non-petroleum resources and usually be regarded as a platform to produce multifarious value-added chemicals. A series of valuable products such as olefins, gasoline, and diesel can be yielded by conventional Fischer–Tropsch (FT) synthesis [4–6], but aromatics can rarely be obtained [7,8]. The combination of FT catalyst with H-ZSM-5 zeolite, such as Fe-MnO/GaZSM-5 [9], Fe-Pd/H-ZSM-5 [10], Na-Zn-Fe_5C_2/H-ZSM-5 [11], and Fe_3O_4@MnO_2/H-ZSM-5 [12], is an effective method to facilitate the synthesis of aromatics. Nevertheless, their aromatics selectivity is still unsatisfactory [9–12].

Recently, a useful approach by employing bifunctional composite catalysts (consisting of oxide and zeolite components), has been successfully utilized in selective conversion of syngas to light olefins [13–17] or liquid fuels [18]. Inspiring by these pioneering works, this strategy has also been used in STA reaction. Wang et al. [19] reported around 20% CO conversion with 80% aromatics selectivity can be obtained over Zn–ZrO_2&H-ZSM-5 composite catalyst. Meanwhile, Bao et al. [20] reported about 73.9% aromatics selectivity with 16% CO conversion over $ZnCrO_x$&H-ZSM-5. Wei et al. [21] reported CO conversion reached to 37% with 70% aromatics selectivity using $ZnCr_2O_4$&-Sbx-H-ZSM-5. The research progress on STA reaction was also reviewed lately [1,22,23]. Although the selectivity of aromatics reported in these studies can exceed 70% frequently, the CO conversion is generally low (Fig S1) [1,19–30]. Up to now, realizing high CO conversion and high aromatics selectivity simultaneously in STA reaction, which is beneficial to decrease the energy consumption for separation products and increase the atom economy, is still challenging.

Herein, we report a 57.5% CO conversion along with 74% aromatics selectivity over a highly effective composite catalyst consisting of $Fe/ZnCr_2O_4$ (Fe modified $ZnCr_2O_4$ spinel) oxide and H-ZSM-5 zeolite. This CO conversion is much higher than those in the previous literature on selective conversion of syngas to more than 70% aromatics.

2. Experimental

2.1. Catalyst preparation

The $ZnCr_2O_4$ spinel oxide was synthesized using a traditional co-precipitation method. Typically, solution A was made by dis-

* Corresponding authors.
E-mail addresses: wlzhu@dicp.ac.cn (W. Zhu), liuzm@dicp.ac.cn (Z. Liu).

https://doi.org/10.1016/j.jechem.2021.03.044

solving 16 g of $Cr(NO_3)_3{\cdot}9H_2O$ and 5.95 g of $Zn(NO_3)_2{\cdot}6H_2O$ in 150 mL of deionized water, and solution B was prepared by dissolving 23.55 g of ammonium carbonate $(NH_4)_2CO_3$ in 150 mL of deionized water. Subsequently, solution A and solution B were simultaneously dropped into a beaker for precipitation at 343 K under continuous stirring. The pH value of the mixed solution was kept at 7.0～7.2 by regulating the flow rate of the two solutions. Then the obtained precipitate continued to age at the same temperature for 3 h. After being filtered and washed thoroughly with deionized water, the resulting mixture was dried overnight at 383 K and finally following calcination in air at 773 K for 4 h.

The $Fe/ZnCr_2O_4$ oxide catalyst was prepared by employing a conventional impregnation method. In brief, solution C was made by dissolving 0.46 g of $Fe(NO_3)_3{\cdot}9H_2O$ in 2 mL of deionized water, then it was dropped onto 2.0 g of $ZnCr_2O_4$ spinel oxide synthesized aforementioned. After being stirred uniformly and placed for 4 h, the resultant mixture was dried at 383 K overnight and finally following calcination at 623 K for 4 h. The obtained powder oxide with about 3.0 wt% of Fe was named as $Fe/ZnCr_2O_4$. H-ZSM-5 zeolite (Si/Al = 96) was identical to that in our recent work [25,32].

The composite catalyst was obtained by a typical physical mixing method. The mass ratio of the two components (oxides and zeolites) was 3:1 unless otherwise stated. For example, for the preparation of the composite catalyst $Fe/ZnCr_2O_4$&H-ZSM-5 (homogeneously mixing), $Fe/ZnCr_2O_4$ oxide and H-ZSM-5 zeolite were put together in an agate mortar and ground evenly, then pressed under 40 MPa and finally sieved to granules with the required size of 0.3～0.45 mm.

For the preparation of the catalyst $Fe/ZnCr_2O_4$ + H-ZSM-5 (granules mixing), $Fe/ZnCr_2O_4$ oxide was put in an agate mortar and ground evenly, then pressed under 40 MPa and sieved to granules with the required size of 0.3～0.45 mm. Subsequently, H-ZSM-5 zeolite also followed the same procedure as $Fe/ZnCr_2O_4$ oxide to obtain granules with the required size of 0.3～0.45 mm. Finally, the granules of the two components ($Fe/ZnCr_2O_4$ oxide and H-ZSM-5 zeolite) were blended together with the mass ratio of 3:1.

2.2. Characterization of catalysts

The chemical composition of catalysts was determined on a PhilipsMagix-601 X-ray fluorescence (XRF) spectrometer. A PANalytical X'Pert PRO X-ray diffractometer with a Cu Kα radiation source radiation (λ = 1.5406 Å) was utilized to record the X-ray diffraction (XRD) data. The average crystal size of catalysts was calculated according to the Scherrer equation. The BET specific surface areas, micropore volume and average pore width were obtained by N_2 adsorption–desorption at 77 K on a Micromeritics ASAP 2020 system. A Hitachi SU8020 field-emission scanning electron microscope (FE-SEM) was utilized to observe the morphology of catalysts. The transmission electron microscopy images (TEM), high-resolution transmission electron microscopy images (HRTEM), scanning transmission electron microscopy images (STEM), particle size and EDS elemental mappings were obtained using a Titan Themis ETEM G3 microscope. Raman spectroscopy was carried out on a NanoWizard Ultra Speed & inVia Raman imaging microscope system with an excitation wavelength of 532 nm.

The *in situ* near ambient pressure X-ray photoelectron spectroscopy (*in situ* NAP-XPS) was performed on a SPECS EnviroESCA spectrometer. The catalyst powder was firstly pressed into a disc and then placed in a laser-heating sample holder, 1 mbar of syngas ($CO/H_2/Ar$ = 47.5/47.5/5) was introduced into the catalyst at 653 K, before and after which the XPS spectra of the catalyst were measured. The binding energy calibration of all the spectra was carried out using the C 1*s* of 284.8 eV as the reference.

The *in situ* ^{57}Fe Mössbauer spectra in a transmission mode were measured on a MFD-500AV-01 *in situ*/*operado* Fe-57 Mössbauer Spectrometer with a ^{57}Co (Rh) source. In order to improve the signal intensity of the spectra, the catalyst was prepared using enriched isotope of ^{57}Fe. The catalyst powder was placed in the sample chamber and in-situ treated with 0.2 MPa of syngas ($CO/H_2/Ar$ = 47.5/47.5/5) at 623 K. The spectra were recorded at room temperature. Velocity calibration was performed using an α-Fe foil. The parameters of Mössbauer were obtained by fitting the spectra utilizing the Mosswin 4.0i software.

The *in situ* diffuse reflectance infrared Fourier transform spectroscopy (DRIFTS) was conducted on a Bruker Tensor 27 instrument equipped with a MCT detector to monitor the evolution of surface intermediates. Firstly, the sample was placed into a diffuse reflectance infrared cell with a ZnSe window. After pretreating by 30 mL·min^{-1} of H_2/N_2 (H_2/N_2 = 1/5) under 0.1 MPa at 583 K and sweeping with 30 mL·min^{-1} of N_2 under the same conditions, the background spectrum was collected at 653 K. Subsequently, 5 mL min^{-1} of syngas ($H_2/CO/Ar$ = 47.5/47.5/5) was introduced under 0.1 MPa at 653 K and the *in situ* DRIFT spectra were obtained at 16 scans with a resolution of 4 cm^{-1}.

2.3. Catalytic reaction

A fixed-bed stainless steel tubular reactor with 8 mm inner diameter was used to conduct all the reactions. Typically, the catalysts were filled in the reactor and activated at 583 K with pure H_2 for 1 h before the reaction. Then, the feed gas was switched to H_2/CO/Ar (molar ratio = 47.5/47.5/5) and the pressure in the reactor was adjusted to 3.0 MPa with the temperature of the catalyst bed was maintained at 653 K. The Space velocity was 2000 mL g^{-1}h^{-1} (for oxides alone) or 1500 mL g^{-1}h^{-1} (for composite catalysts). The reaction effluent products were heated to keep in the gas phase and analyzed by an online gas chromatograph (Agilent 7890B), which equipped with a flame ionization detector (FID) connected to a PoraPLOT Q-HT capillary column and a thermal conductivity detector (TCD) connected to a TDX-1 packed column. Argon was used as an inner standard gas. CO_2 selectivity and CO conversion were calculated on the basis of the carbon atoms number according to the following formula.

$$Sel_{CO_2} = \frac{CO_{2\,outlet}}{CO_{inlet} - CO_{outlet}} \times 100\% \quad (1)$$

$CO_{2\ outlet}$: moles of CO_2 at the outlet.

$$Conv_{CO} = \frac{(CO_{inlet} - CO_{outlet})}{CO_{inlet}} \times 100\% \quad (2)$$

$CO_{\ inlet}$: moles of CO at the inlet; $CO_{\ outlet}$: moles of CO at the outlet.

The selectivity of hydrocarbons (C_nH_m), DME or MeOH (excluding CO_2) was obtained according to the total carbon moles of the products detected by FID.

$$Sel_{C_nH_m} = \frac{n_{C_nH_m}}{n_{DME} + n_{MeOH} + n_{C_nH_m}} \times 100\%$$

$$Sel_{MeOH} = \frac{n_{MeOH}}{n_{DME} + n_{MeOH} + n_{C_nH_m}} \times 100\%$$

$$Sel_{DME} = \frac{n_{DME}}{n_{DME} + n_{MeOH} + n_{C_nH_m}} \times 100\% \quad (3)$$

n_{CnHm}: carbon moles of C*n*H*m*.

n MeOH: carbon moles of MeOH.

n DME: carbon moles of DME.

The carbon balance was calculated according to the following formula:

$$C_{balance} = \frac{CO_{2\,outlet} + n_{DME} + n_{MeOH} + n_{C_nH_m}}{CO_{inlet} - CO_{outlet}} \times 100\%$$

The carbon balance was over 95% in the reaction.

3. Results and discussion

3.1. Catalytic results

We compared the catalytic results of syngas conversion over $ZnCr_2O_4$ and $Fe/ZnCr_2O_4$ oxides at 653 K, 3.0 MPa, Space velocity = 2000 mL $g^{-1}h^{-1}$ (Fig. 1a and Table S2). The primary products for $ZnCr_2O_4$ are MeOH and DME with a very low CO conversion (3.2%). After introducing about 3.0 wt% of Fe onto $ZnCr_2O_4$ (Table S1), the ability of CO activation improves greatly and a CO conversion of 17.1% was obtained. Apart from a small amount of MeOH and DME, CH_4 dominated the major products over $Fe/ZnCr_2O_4$, which can be ascribed to the over hydrogenation of some C_1 oxygenated intermediates [27,31]. It also can be seen from Fig. 1a and Table S2 that the combination of these oxides with H-ZSM-5 zeolite can obviously facilitate the CO conversion and the formation of aromatics. $ZnCr_2O_4$&H-ZSM-5 exhibits 73.4% aromatics in the products excluding CO_2 with 20.8% CO conversion. Surprisingly, the CO conversion reaches to 35.2% over $Fe/ZnCr_2O_4$&H-ZSM-5 without sacrificing the aromatics selectivity and changing the distribution of aromatics (Fig S2). Besides, after introducing about 3 wt% of Fe onto $ZnCr_2O_4$, the CO conversion can be enhanced greatly at every reaction temperature without decreasing the selectivity of aromatics (Fig S3). Moreover, as shown in Fig. 1b, the aromatics formation rate can also be improved significantly. This suggests that the introduction of Fe not only promotes the conversion of CO but also does not depress the generation of aromatics.

We further studied the catalytic results over $Fe/ZnCr_2O_4$&H-ZSM-5 composite catalyst under different reaction conditions. As shown in Fig. 2a and Table S3, higher H_2/CO ratio is advantageous to the CO conversion, while lower H_2/CO ratio is beneficial for the formation of aromatics. The increase of reaction pressure helps to facilitate CO conversion and synthesis of aromatics (Fig. 2b and Table S3). The CO conversion reaches to 45.5% with 71.6% aromatics selectivity at 5 MPa. Raising the space velocity can lead to diminishing the aromatics but increasing the MeOH, DME and light olefins, indicating that these species may act as the intermediates for generating aromatics (Fig. 2c and Table S3) [32]. Notably, as high as 57.5% CO conversion along with 74% selectivity of aromatics can be achieved at space velocity = 500 mL $g^{-1}h^{-1}$ (Fig. 2c, Fig. S4 and Table S3). To the best of our knowledge, when the aromatics selectivity is greater than 70%, this CO conversion achieves the highest value reported among the previous literature on syngas conversion to aromatics (Fig. S1) [19–30]. The optimal mass ratio of $Fe/ZnCr_2O_4$ oxide and H-ZSM-5 zeolite is 3:1 (Fig. S5). Increasing the proximity of oxide and zeolite can not only promote the conversion of CO, but also facilitate the further conversion of some C_1 oxygenated intermediates to synthesize aromatics in zeolite, thus avoiding the over hydrogenation on oxide (Fig. S6) [27]. In addition, the $Fe/ZnCr_2O_4$&H-ZSM-5 composite catalyst exhibits a good stability in a 100 h test (Fig. 2d). Moreover, the CO_2 selectivity is between 40%~50% (Fig. 2a-d and Table S3), which can attribute to the water–gas shift (WGS) reaction: $CO + H_2O \rightarrow CO_2 + H_2$ [19,20,22,33].

3.2. Structural characterization

The diffraction peaks in XRD patterns (Fig. 3a) of $ZnCr_2O_4$ and $Fe/ZnCr_2O_4$ oxides are all consistent with the typical cubic $ZnCr_2O_4$ spinel structure. No significant phases related to Fe are observed, suggesting the Fe species are highly dispersed in $ZnCr_2O_4$ oxides [34]. The *In situ* NAP-XPS spectra of the Zn 2*p* and Cr 2*p* for $ZnCr_2O_4$ and $Fe/ZnCr_2O_4$ oxides (Fig. S7) all mainly present the characteristic peak of Zn^{2+} (Zn 2*p*3/2: 1021.5 ± 0.3 eV) [35] and Cr^{3+} (Cr 2*p*3/2: 576.4 ± 0.3 eV) [36] during the syngas reaction, which fully agree with the valence state of Zn and Cr in the cubic $ZnCr_2O_4$ spinel. The introduction of a small amount of Fe will not have an obvious influence on the physical property of $ZnCr_2O_4$ (Table S1). The FE-SEM images (Fig. 3b and Fig. S9) display that $ZnCr_2O_4$ and $Fe/ZnCr_2O_4$ oxides are composed of irregular nanoparticles with a size of 10–20 nm, between which the stacked mesoporous was formed (Fig. S8). The TEM image (Fig. 3c) also shows that $Fe/ZnCr_2O_4$ consists of nanoparticles with a particle-size distribution of 11.14 ± 1.7 nm, which almost agrees with the average crystal size estimated by the Scherrer equation (Table S1). The lattice fringe spaced of 0.481 nm and 0.252 nm in HRTEM images (Fig. 3d and Fig. S10) can be assigned to the (111) and (113) planes of $ZnCr_2O_4$ spinel, no obvious Fe clustering can be discovered. The EDS mappings in Fig. S11 further illustrate the high dispersion of Fe in $ZnCr_2O_4$ spinel, which is also in accordance with the XRD results (Fig. 3a). Besides, after syngas reaction, $Fe/ZnCr_2O_4$ oxide maintains a cubic $ZnCr_2O_4$ spinel structure and above which the Fe species are still highly dispersed (Fig. S12).

As observed in Fig. 4a, the O 1*s* XPS spectra of $ZnCr_2O_4$ and $Fe/ZnCr_2O_4$ oxides can be clearly identified into two peaks. One peak located at a lower binding energy of about 530 eV can be deemed as the lattice oxygen atoms ($O_{lattice}$) [37], while the other peak situated at a higher binding energy of around 531 eV can be generally regarded as the oxygen atoms in the vicinity of the oxygen vacancy ($O_{vacancy}$) [16,38]. On the basis of the results calculated from the

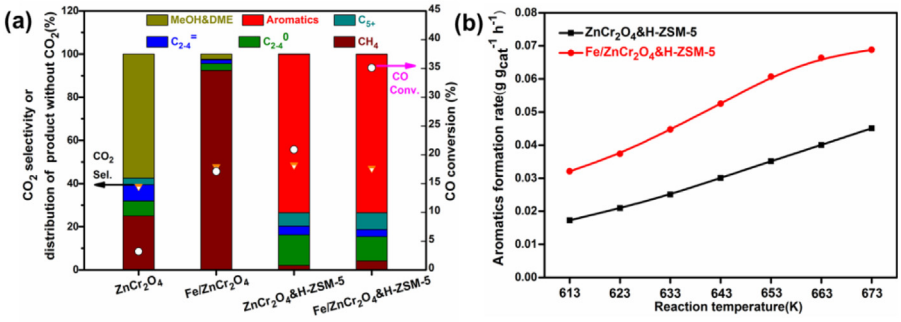

Fig. 1. Catalytic results for syngas conversion. (a) Syngas conversion over oxides and composite catalysts. 653 K, 3.0 MPa, $H_2/CO/Ar$ (molar ratio) = 47.5/47.5/5, Space velocity = 2000 mL $g^{-1}h^{-1}$ for oxides or 1500 mL $g^{-1}h^{-1}$ for composite catalysts. (b) The effect of reaction temperature on aromatics formation rate over composite catalysts. 3.0 MPa, $H_2/CO/Ar$ = 47.5/47.5/5, Space velocity = 1500 mL $g^{-1}h^{-1}$. Note that $C_{2-4}^{=}$ and C_{2-4}^{0} refer to C_{2-4} olefins and paraffins, respectively. The C_{5+} excludes aromatics. The aromatics formation rate is gram of aromatics generated on per gram of composite catalysts per hour.

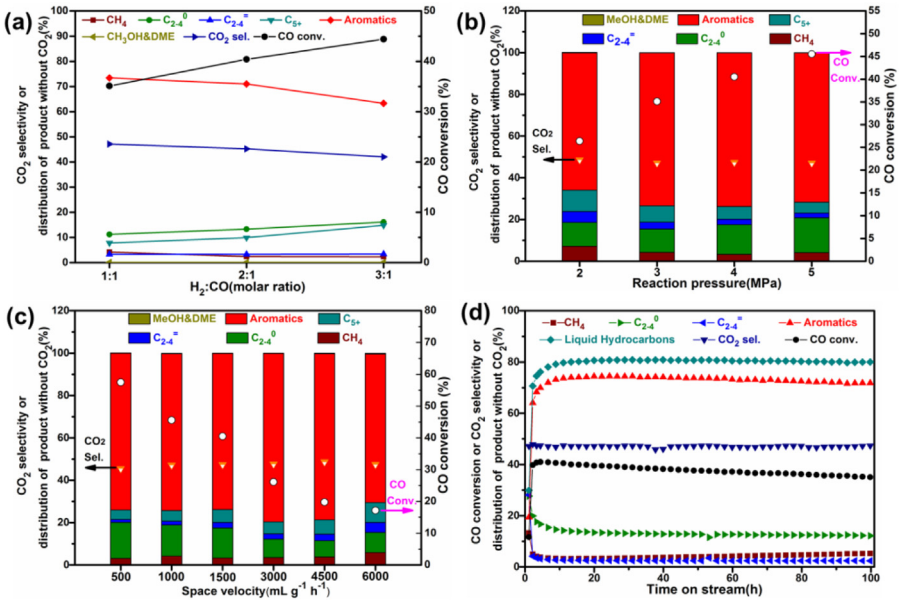

Fig. 2. Catalytic results for syngas conversion. (a) The effect of H_2/CO molar ratio on syngas conversion over Fe/$ZnCr_2O_4$&H-ZSM-5 composite catalyst. 653 K, 3.0 MPa, space velocity = 1500 mL $g^{-1}h^{-1}$. (b) The effect of reaction pressure on syngas conversion over Fe/$ZnCr_2O_4$&H-ZSM-5 composite catalyst. 653 K, H_2/CO/Ar (molar ratio) = 47.5/47.5/5, space velocity = 1500 mL $g^{-1}h^{-1}$. (c) The effect of space velocity on syngas conversion over Fe/$ZnCr_2O_4$&H-ZSM-5 composite catalyst. 653 K, 4.0 MPa, H_2/CO/Ar (molar ratio) = 47.5/47.5/5. (d) The stability test for Fe/$ZnCr_2O_4$&H-ZSM-5 composite catalyst. 653 K, 4.0 MPa, H_2/CO/Ar (molar ratio) = 47.5/47.5/5, space velocity = 1500 mL $g^{-1}h^{-1}$. Note that $C_{2-4}^{=}$ and C_{2-4}^{0} refer to C_{2-4} olefins and paraffins, respectively. The C_{5+} excludes aromatics. The liquid hydrocarbons include C_5^+ and aromatics.

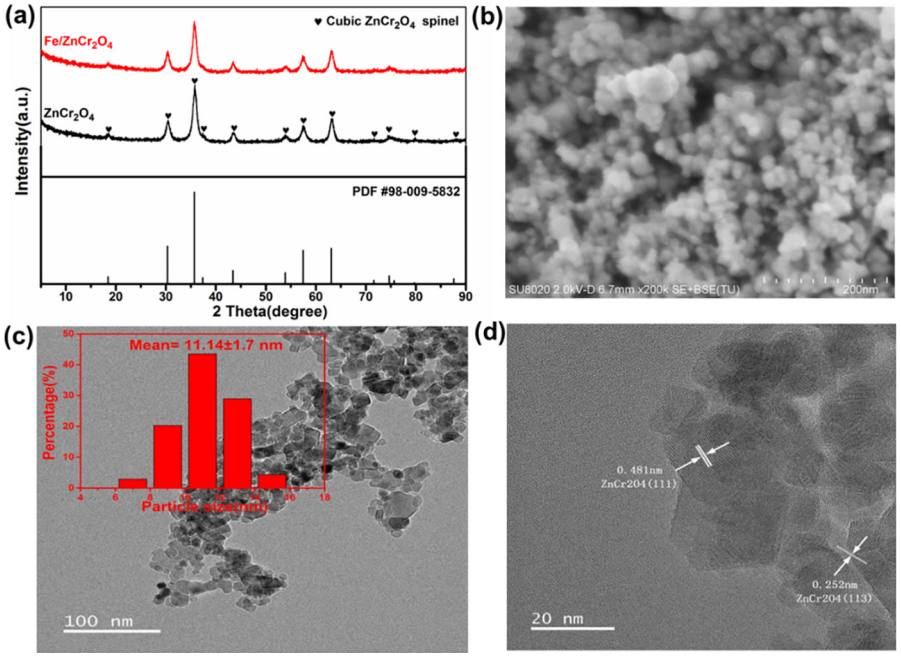

Fig. 3. Structural characterization of oxides. (a) XRD patterns of oxides. (b) The FE-SEM image of Fe/$ZnCr_2O_4$. (c) The TEM image and particle-size distribution of Fe/$ZnCr_2O_4$. (d) The HRTEM image of Fe/$ZnCr_2O_4$.

deconvolution of O 1*s* XPS signal (Table S4 and inset in Fig. 4a) [39], the introduction of Fe onto $ZnCr_2O_4$ can induce an increase of oxygen vacancy concentration and it reaches up to 48% for Fe/$ZnCr_2O_4$. As known, the increase of oxygen vacancy concentration is conducive to promoting the activation of CO to form more intermediates, which can be further transformed to propel the formation of aromatics [24,25,40].

The *in situ* NAP-XPS spectra of the Fe 2*p* were employed to further investigate the detailed surface nature of Fe/$ZnCr_2O_4$ during the reaction process. As shown in Fig. 4b, for the fresh Fe/$ZnCr_2O_4$ under ultrahigh vacuum at room temperature, Fe 2*p*3/2 and Fe 2*p*1/2 peaks are discriminated at around 711.4 eV and 724.3 eV, respectively, which can be attributed to the characteristic of Fe^{3+} [12,15]. Notably, a new peak located at about 706.5 eV appeared under 1 mbar of syngas at 653 K, corresponding to the characteristic of iron carbide species [15,41,42]. In addition, Raman spectra (Fig. S13) reveal that the G band peak (1607 cm^{-1}) and D band peak (1350 cm^{-1}) increased significantly for the Fe/$ZnCr_2O_4$ after

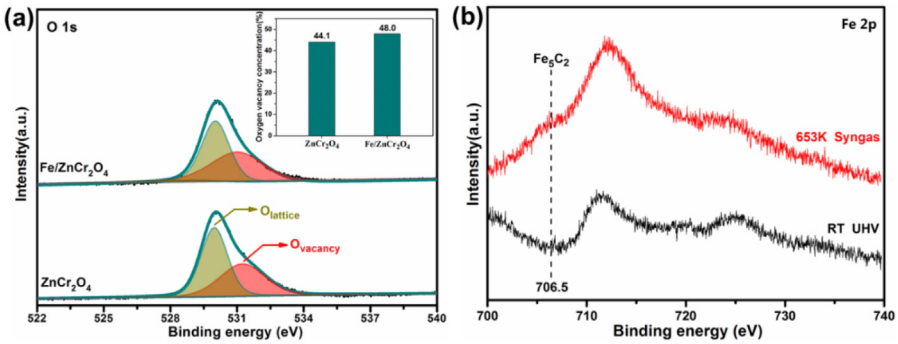

Fig. 4. Structural characterization of oxides. (a) The O 1*s* XPS spectra of oxides. $O_{lattice}$ denoted as the lattice oxygen atoms, $O_{vacancy}$ denoted as the oxygen atoms adjacent to the oxygen vacancy. The inset is the oxygen vacancy concentration of oxides calculated from the deconvolution of O 1*s* XPS signal (for a detailed description, see Table S4 in the Supporting Information). (b) The *in situ* NAP-XPS spectra of the Fe 2*p* for $Fe/ZnCr_2O_4$ surface. The black curve is corresponding to the fresh sample under ultrahigh vacuum (UHV) at room temperature, the red curve is corresponding to the sample under 1 mbar of syngas ($CO/H_2/Ar$ = 47.5/47.5/5) at 653 K.

reaction, which can be ascribed to the carbonaceous species on the iron carbide surface [12,41]. Furthermore, the *in situ* ^{57}Fe Mössbauer spectra (Table S5) also suggest there may be the formation of iron carbide species during the reaction process. It is well known that the iron carbide species are beneficial to facilitate CO activation [4,12,15,41]. According to the findings above, we speculate that $Fe/ZnCr_2O_4$ spinel oxide with higher oxygen vacancy concentration and highly dispersed iron carbide species formed during the reaction, can be responsible for the enhancement in catalytic activity without sacrificing the selectivity of aromatics.

In order to gain further insights into the reaction mechanism, the evolution of surface intermediates was monitored by the *in situ* diffuse reflectance infrared Fourier transform spectroscopy (DRIFTS). As shown in Fig. 5a, the adsorbed surface carbonate/bicarbonate species (1492, 1380 and 1305 cm^{-1}) [16,31,43], formate species (2957, 2867, 2743, 1580 and 1357 cm^{-1}) [17,28,31,43] and methoxy species (2927 and 2815 cm^{-1}) [17,28,31,43] are distinctly observed for $ZnCr_2O_4$ oxide under reaction condition, and the intensity of IR bands for these oxygenated intermediate species is improved as the syngas adsorption time increased from 1 to 30 min. After combining $ZnCr_2O_4$ oxide with H-ZSM-5 zeolite, the characteristic bands of these surface oxygenated intermediate species almost completely disappeared (Fig. 5c), which implies these active surface intermediates generated over $ZnCr_2O_4$ can be converted by H-ZSM-5 [28,31,32]. Remarkably, comparing with $ZnCr_2O_4$, the formation of these surface oxygenated intermediate species over $Fe/ZnCr_2O_4$ is obviously more quickly, and the intensity of corresponding characteristic bands for these intermediates is also significantly enhanced (Fig. 5b). Furthermore, due to adequate surface oxygenated intermediate species being generated, these intermediates can even be detected over $Fe/ZnCr_2O_4$&H-ZSM-5 composite catalyst (Fig. 5d). These findings coincide with the catalytic performance in Fig. 1 and further verify the high activity of $Fe/ZnCr_2O_4$.

On the basis of results found above and previous studies from literature, we propose a possible reaction mechanism for the

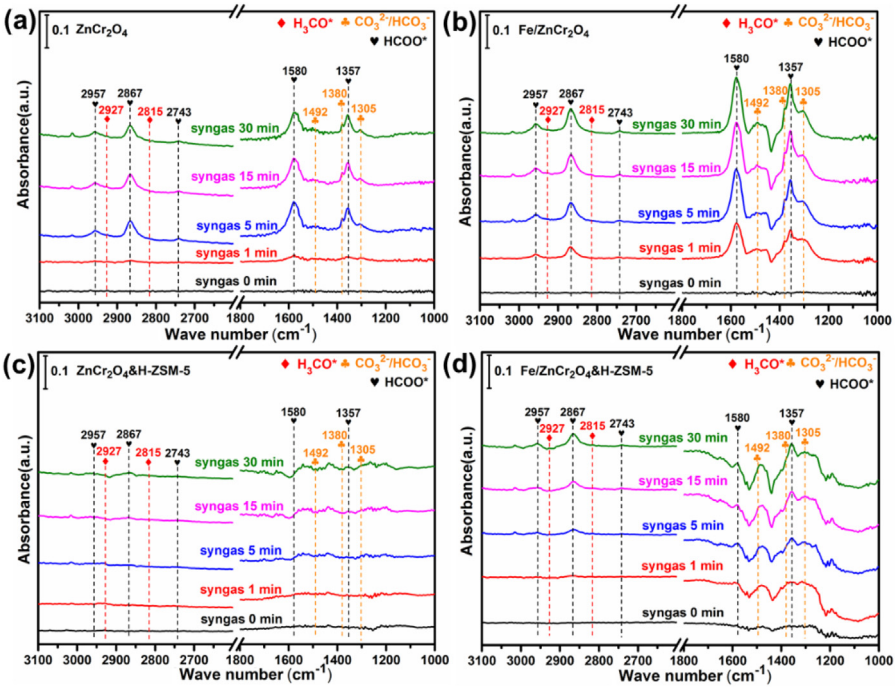

Fig. 5. *In situ* DRIFT spectra for various catalysts. *In situ* DRIFT spectra for (a) the CO hydrogenation over $ZnCr_2O_4$ oxide, (b) the CO hydrogenation over $Fe/ZnCr_2O_4$ oxide, (c) the CO hydrogenation over $ZnCr_2O_4$&H-ZSM-5 composite catalyst, and (d) the CO hydrogenation over $Fe/ZnCr_2O_4$&H-ZSM-5 composite catalyst. Reaction conditions: 653 K, 0.1 MPa, syngas refers to the mixed gas of $CO/H_2/Ar$ = 47.5/47.5/5.

hydrogenation of CO over Fe/$ZnCr_2O_4$&H-ZSM-5 composite catalyst. The introduction of Fe onto $ZnCr_2O_4$ can induce an increase of oxygen vacancy concentration (Fig. 4a). Meanwhile, there is some highly dispersed iron carbide species formed over $ZnCr_2O_4$ spinel during the reaction (Fig. 4b). They together significantly facilitate the CO hydrogenation activation [4,12,15,24,25,40,41], resulting in a rapid formation of more oxygenated intermediate species (carbonate/bicarbonate, formate and methoxy species) (Fig. 5). These active oxygenated intermediates can be further converted to generate MeOH, DME and olefins intermediates [17,28,32,43], or/and carbonyl compounds intermediates [31,44], which can be continuously transformed to produce aromatics in H-ZSM-5 finally [31,32,43,44]. As a consequence, high CO conversion and high aromatics selectivity can be achieved simultaneously.

4. Conclusion

In summary, a 57.5% CO conversion along with 74% aromatics selectivity was achieved over Fe/$ZnCr_2O_4$&H-ZSM-5 composite catalyst at 653 K under 4.0 MPa. To the best of our knowledge, this CO conversion is much higher than those in the previous literature on selective conversion syngas to more than 70% aromatics. Compared with conventional $ZnCr_2O_4$&H-ZSM-5, impregnation of only 3 wt% of Fe on to $ZnCr_2O_4$ can significantly increase the CO conversion without sacrificing the aromatics selectivity. Oxygen vacancy concentration is obviously improved after impregnating Fe. The highly dispersed iron carbide species formed during the reaction over Fe/$ZnCr_2O_4$ spinel oxide. The synergistic effect of oxygen vacancy and iron carbide results in a rapid formation of abundant oxygenated intermediate species, which can be continuously transformed to aromatics in H-ZSM-5. This type of composite catalyst suggests a promising application in syngas conversion.

Declaration of Competing Interest

The authors declare that they have no known competing financial interests or personal relationships that could have appeared to influence the work reported in this paper.

Acknowledgments

We acknowledge the financial support from the National Natural Science Foundation of China (Grant No. 21978285, 21991093, 21991090), the "Transformational Technologies for Clean Energy and Demonstration", and the Strategic Priority Research Program of the Chinese Academy of Sciences (Grant No. XDA21030100). We acknowledge Mrs. Yanli He and Mr. Yijun Zheng for their help in the characterization of catalysts. We acknowledge Prof. Peng Guo for his kind assistance in the test of TEM. Prof. Junhu Wang and Dr. Rile Ge are acknowledged for their help in the measurement and discussion of *in situ* ^{57}Fe Mössbauer spectra.

Appendix A. Supplementary data

Supplementary data to this article can be found online at https://doi.org/10.1016/j.jechem.2021.03.044.

References

[1] X.L. Yang, X. Su, D. Chen, T. Zhang, Y.Q. Huang, Chin. J. Catal. 41 (2020) 561–573.
[2] A.M. Niziolek, O. Onel, Y.A. Guzman, C.A. Floudas, Energy Fuels 30 (2016) 4970–4998.
[3] Y.M. Jia, J.W. Wang, K. Zhang, S.B. Liu, G.L. Chen, Y.F. Yang, C.M. Ding, P. Liu, Catal, Sci. Technol. 7 (2017) 1776–1791.
[4] H.M.T. Galvis, J.H. Bitter, C.B. Khare, M. Ruitenbeek, A.I. Dugulan, K.P. de Jong, Science 335 (2012) 835–838.
[5] H.M.T. Galvis, K.P. de Jong, ACS Catal. 3 (2013) 2130–2149.
[6] L.S. Zhong, F. Yu, Y.L. An, Y.H. Zhao, Y.H. Sun, Z.J. Li, T.J. Lin, Y.J. Lin, X.Z. Qi, Y.Y. Dai, L. Gu, J.S. Hu, S.F. Jin, Q. Shen, H. Wang, Nature 538 (2016) 84–87.
[7] R.A. Friedel, R.B. Anderson, J. Am. Chem. Soc. 72 (1950) 1212–1215.
[8] M.E. Dry, J. Chem. Technol. Biotechnol. 77 (2002) 43–50.
[9] N. Guan, Y. Liu, M. Zhang, Catal. Today 30 (1996) 207–213.
[10] Q.G. Yan, Y.W. Lu, C.X. Wan, J. Han, J. Rodriguez, J.J. Yin, F. Yu, Energy Fuels 28 (2014) 2027–2034.
[11] B. Zhao, P. Zhai, P.F. Wang, J.Q. Li, T. Li, M. Peng, M. Zhao, G. Hu, Y. Yang, Y.W. Li, Q.W. Zhang, W.B. Fan, D. Ma, Chem 3 (2017) 323–333.
[12] Y. Xu, J. Liu, J. Wang, G. Ma, J. Lin, Y. Yang, Y. Li, C. Zhang, M. Ding, ACS Catal. 9 (2019) 5147–5156.
[13] F. Jiao, J.J. Li, X.L. Pan, J.P. Xiao, H.B. Li, H. Ma, M.M. Wei, Y. Pan, Z.Y. Zhou, M.R. Li, S. Miao, J. Li, Y.F. Zhu, D. Xiao, T. He, J.H. Yang, F. Qi, Q. Fu, X.H. Bao, Science 351 (2016) 1065–1068.
[14] K. Cheng, B. Gu, X.L. Liu, J.C. Kang, Q.H. Zhang, Y. Wang, Angew. Chem. Int. Ed. 55 (2016) 4725–4728.
[15] P. Zhai, C. Xu, R. Gao, X. Liu, M.Z. Li, W.Z. Li, X.P. Fu, C.J. Jia, J.L. Xie, M. Zhao, X.P. Wang, Y.W. Li, Q.W. Zhang, X.D. Wen, D. Ma, Angew. Chem. Int. Ed. 55 (2016) 9902–9907.
[16] Y.F. Zhu, X.L. Pan, F. Jiao, J. Li, J.H. Yang, M.Z. Ding, Y. Han, Z. Liu, X.H. Bao, ACS Catal. 7 (2017) 2800–2804.
[17] X.L. Liu, W. Zhou, Y.D. Yang, K. Cheng, J.C. Kang, L. Zhang, G.Q. Zhang, X.J. Min, Q.H. Zhang, Y. Wang, Chem. Sci. 9 (2018) 4708–4718.
[18] N. Li, F. Jiao, X.L. Pan, Y.X. Chen, J.Y. Feng, G. Li, X.H. Bao, Angew. Chem. Int. Ed. 58 (2019) 7400–7404.
[19] K. Cheng, W. Zhou, J.C. Kang, S. He, S.L. Shi, Q.H. Zhang, Y. Pan, W. Wen, Y. Wang, Chem 3 (2017) 334–347.
[20] J.H. Yang, X.L. Pan, F. Jiao, J. Li, X.H. Bao, Chem. Commun. 53 (2017) 11146–11149.
[21] M.T. Arslan, B.A. Qureshi, S.Z.A. Gilani, D.L. Cai, Y.H. Ma, M. Usman, X. Chen, Y. Wang, F. Wei, ACS Catal. 9 (2019) 2203–2212.
[22] W. Zhou, K. Cheng, J. Kang, C. Zhou, V. Subramanian, Q. Zhang, Y. Wang, Chem. Soc. Rev. 48 (2019) 3193–3228.
[23] S. Kasipandi, J.W. Bae, Adv. Mater. 31 (2019) 1803390.
[24] Z. Huang, S. Wang, F. Qin, L. Huang, Y.H. Yue, W.M. Hua, M.H. Qiao, H.Y. He, W. Shen, H.L. Xu, ChemCatChem 10 (2018) 4519–4524.
[25] Y. Fu, Y.M. Ni, W.L. Zhu, Z.M. Liu, J. Catal. 383 (2020) 97–102.
[26] W. Zhou, S.L. Shi, Y. Wang, L. Zhang, Y. Wang, G.Q. Zhang, X.J. Min, K. Cheng, Q. H. Zhang, J.C. Kang, Y. Wang, ChemCatChem 11 (2019) 1681–1688.
[27] X.L. Yang, T. Sun, J.G. Ma, X. Su, R.F. Wang, Y.R. Zhang, H.M. Duan, Y.Q. Huang, T. Zhang, J. Energy Chem. 35 (2019) 60–65.
[28] Y.J. Wang, W.T. Zhan, Z.J. Chen, J.M. Chen, X.G. Li, Y.W. Li, ACS Catal. 10 (2020) 7177–7187.
[29] J.G. Liu, Y.R. He, L.L. Yan, K. Li, C.H. Zhang, H.W. Xiang, X.D. Wen, Y.W. Li, Catal, Sci. Technol. 9 (2019) 2982–2992.
[30] D.Y. Miao, Y. Ding, T. Yu, J. Li, X.L. Pan, X.H. Bao, ACS Catal. 10 (2020) 7389–7397.
[31] M.T. Arslan, B. Ali, S.Z.A. Gilani, Y.L. Hou, Q. Wang, D.L. Cai, Y. Wang, F. Wei, ACS Catal. 10 (2020) 2477–2488.
[32] Y.M. Ni, Z.Y. Chen, Y. Fu, Y. Liu, W.L. Zhu, Z.M. Liu, Nat. Commun. 9 (2018) 3457.
[33] W. Zhou, C. Zhou, H.R. Yin, J.Q. Shi, G.Q. Zhang, X.L. Zheng, X.J. Min, Z.Q. Zhang, K. Cheng, J.C. Kang, Q.H. Zhang, Y. Wang, Chem. Commun. 56 (2020) 5239–5242.
[34] Q. Ling, M. Yang, C.S. Li, A.M. Zhang, RSC Adv. 4 (2014) 4020–4027.
[35] X.T. Zhou, T.H. Lin, Y.H. Liu, C.X. Wu, X.Y. Zeng, D. Jiang, Y.A. Zhang, T.L. Guo, A. C.S. Appl, Mater. Interfaces 5 (2013) 10067–10073.
[36] Y.Y. Li, J. Hu, J. Xu, Y.P. Zheng, M.S. Chen, H.L. Wan, Q. Fu, F. Yang, X.H. Bao, Appl. Surf. Sci. 494 (2019) 353–360.
[37] C. Yang, J. Wang, H.L. Fan, S.G. Ju, J. Mi, C. Huo, Fuel 215 (2018) 695–703.
[38] F.C. Lei, Y.F. Sun, K.T. Liu, S. Gao, L. Liang, B.C. Pan, Y. Xie, J. Am. Chem. Soc. 136 (2014) 6826–6829.
[39] Z.L. Wang, X. Mao, P. Chen, M. Xiao, S.A. Monny, S.C. Wang, M. Konarova, A.J. Du, L.Z. Wang, Angew. Chem., Int. Ed. 58 (2019) 1030–1034.
[40] X.L. Liu, M.H. Wang, C. Zhou, W. Zhou, K. Cheng, J.C. Kang, Q.H. Zhang, W.P. Deng, Y. Wang, Chem. Commun. 54 (2018) 140–143.
[41] C. Yang, H.B. Zhao, Y.L. Hou, D. Ma, J. Am. Chem. Soc. 134 (2012) 15814–15821.
[42] Q.J. Chen, G.G. Liu, S.Y. Ding, M.C. Sheikh, D.H. Long, Y. Yoneyama, N. Tsubaki, Chem. Eng. J. 334 (2018) 714–724.
[43] C. Zhou, J.Q. Shi, W. Zhou, K. Cheng, Q.H. Zhang, J.C. Kang, Y. Wang, ACS Catal. 10 (2020) 302–310.
[44] Z.Y. Chen, Y.M. Ni, F.L. Wen, Z.Q. Zhou, W.L. Zhu, Z.M. Liu, Chin. J. Catal. 42 (2021) 835–843.